Five-Wavelength-Switchable Single-Longitudinal-Mode Thulium-Doped Fiber Laser Based on a Passive Cascaded Triple-Ring Cavity Filter

Dan Cheng, Fengping Yan, Ting Feng, Wenguo Han, Luna Zhang, Qi Qin, Ting Li, Zhuoya Bai, Dandan Yang, Ying Guo, and Wei Wang

***Abstract*—A five-wavelength-switchable thulium-doped fiber laser with a fiber Bragg grating (FBG)-based five-channel transmitting Fabry-Pérot (F-P) filter and a multi-coupler based triple-ring cavity (CTRC) filter, is experimentally proposed. For the first time, a multi-channel F-P filter and specially-designed coupler-based compound cavity filter were combined to realize multi-wavelength-switchable operation, with single-longitudinal-mode (SLM) lasing for each wavelength channel in a 2 μm band fiber laser. The theoretical analysis of the CTRC filter and the principle for achieving SLM operation by corporately using the F-P filter and CTRC filter were presented in detail. The experimental results demonstrated the good performance of the proposed filters. Five lasing wavelengths (1941.13 nm, 1941.22 nm, 1941.30 nm, 1941.39 nm, and 1941.47 nm) were obtained with good switchability, and each operated in a stable SLM state. The OSNR of each lasing wavelength was higher than 50 dB, and the linewidths of all obtained wavelengths were less than 8 kHz.**

***Index Terms*—Thulium-doped fiber laser, single longitudinal mode, laser linewidth, fiber Bragg grating.**

I. Introduction

SINGLE-longitudinal-mode (SLM) fiber lasers have drawn intense research interest because they provide a narrow-linewidth, low relative intensity noise, and high beam quality output. These inherent merits make such lasers preferable for applications in spectroscopy, Doppler LIDAR, radio-over-fiber, etc. [1]–[4]. According to the total cavity length, the SLM fiber laser configurations can be classified into the short-cavity structure, which includes distributed feedback (DFB) lasers[5] and distributed Bragg reflection (DBR) fiber lasers[6], and long-cavity structures with proper mode selection mechanisms [7]. DFB and DBR lasers provide compactness structure and robust SLM operation; however, they suffer from relatively low laser efficiencies due to the short length of the gain fiber. When it comes to laser flexibility and tunability, long-cavity lasers embedded mode selectors are the laser of choice over any other short-cavity lasers. There is no cavity length limitation, which enables the tunable components to be installed inside the cavity. Moreover, the cavity can accommodate a sufficiently long active fiber to obtain the desired gain.

To achieve SLM oscillation in long-cavity lasers, it is critical to find effective mode selection mechanisms against the resulting small FSR due to the increased fiber length. Many mode-selection techniques have been proposed, which can be sorted into three main types. One is the combined use of ultra-narrow bandwidth filters and wavelength selection mechanisms [8]–[10]. The second involves incorporating an unpumped doped fiber as the saturable absorber in the cavity to prevent multi-mode operation and stabilize the laser [11], [12]. The third is to combine the wavelength selector in the compound-cavity or multi-ring compound cavity (MR-CC). In this method, the fiber rings based on optical couplers (OCs) serve as passive subring cavities to expand the effective FSR of the compound cavity according to the Vernier effect [13], [14]. Then, SLM operation can be obtained when the effective FSR is wider than half the 3 dB-bandwidth of the wavelength selector [15]. The primary passive subring cavities in an MR-CC are generally composed of one or multi-cascaded/parallel single-coupler-based fiber rings (single-coupler ring, SCR) [16]–[18], dual-coupler ring (DCR) [13], [16], three nested couplers ring[19], or a combination of DCR and SCR [20]. Apart from quantitatively determining the parameters of compound rings based on the Vernier effect, the filtering performance for the desired mode can also be determined by obtaining the optimized parameters

Manuscript received October 7, 2021; revised November 7, 2021; accepted November 11, 2021. Date of publication November 15, 2021; date of current version December 7, 2021. This work was supported in part by the National Natural Science Foundation of China under Grants 61827818, 61620106014, and 61975049, and in part by the Hebei Provincial Natural Science Foundation for Outstanding Young Scholars under Grant F2020201001. *(Corresponding authors: Fengping Yan; Ting Feng.)*

Dan Cheng, Fengping Yan, Wenguo Han, Qi Qin, Ting Li, Zhuoya Bai, Dandan Yang, Ying Guo, and Wei Wang are with the School of Electronic and Information Engineering, Beijing Jiaotong University, Beijing 100044, China (e-mail: dancheng621@hotmail.com; fpyan@bjtu.edu.cn; 14111021@bjtu.edu.cn; 19111034@bjtu.edu.cn; 19111024@bjtu.edu.cn; 16111003@bjtu.edu.cn; 2554332431@qq.com; 18111014@bjtu.edu.cn; 15111006@bjtu.edu.cn).

Ting Feng is with the Photonics Information Innovation Center, Hebei Provincial Center for Optical Sensing Innovations, College of Physics Science & Technology, Hebei University, Baoding 071002, China (e-mail: wlxyft@hbu.edu.cn).

Luna Zhang is with the Key Lab of Solid State Laser, Technical Institute of Physics and Chemistry, Chinese Academy of Sciences, Beijing 100190, China (e-mail: zhangluna@mail.ipc.ac.cn).

Digital Object Identifier 10.1109/JPHOT.2021.3128165

by theoretically and numerically analyzing the influence of the coupler ratio, fiber length, and coupler connection methods. Our group has proposed lasers that showed great SLM lasing performance with specially-designed compound ring-based filters [21], [22].

Using the aforementioned strategies, state-of-the-art SLM laser sources have been intensively reported, and the development of SLM lasers operating at around 2 μm has begun to gather pace. Thulium-doped fiber lasers offer a broad emission range (1660–2200 nm), which falls in the eye-safe spectral region and also covers the atmospheric transparency window where the permissible power transmission for light in free space can be several orders of magnitude higher than other wavelength bands. With these advanced features, a 2 μm SLM fiber laser can be adapted for use in free-space optical communications and laser weapon manufacturing [23]. Due to overlapping with the absorption lines of various atmospheric gas, such as N_2O, H_2O, and CO_2, SLM fiber lasers that operate at around 2 μm can also be widely applied for high-resolution gas sensing; however, there is a shortage of optimized components for use in 2 μm band compared with those in 1.5 μm and 1 μm band. The lack of adequate means of linewidth measurement is also responsible for slowing the speed of developing 2 μm SLM lasers. For the sake of the high transmission loss of 2 μm light in standard single-mode fiber, the traditional delayed self-heterodyne linewidth measurement method with a long delay line is no longer the most suitable strategy for measuring linewidths in 2 μm band. Currently, the proposed SLM lasers at 2 μm are mainly based on the short-cavity structure [24], and there are few reports on long-cavity-structure based tunable or switchable SLM lasers at 2 μm [25], [26]; however, previously reported compound-cavity filters were not completely analyzed or quantitatively designed in detail. Furthermore, coupler-based compound-cavity filters are more affordable and easy-alternative than other filters for realizing SLM lasing in 2 μm band. For these reasons, it is meaningful to realize multi-wavelength-switchable SLM lasers and utilize compound-cavity filters in laser cavities in 2 μm band.

In this work, we present a five-wavelength-switchable SLM fiber laser operating in 2 μm band. In the proposed laser configuration, a homemade FBG based F-P acts as the narrow bandwidth five-channel filter. Each wavelength in the channel can be filtered out by a tunable FBG. In addition, a specially-designed cascaded triple-ring cavity (CTRC) was embedded to realize mode selection and ensure the SLM operation of each selected wavelength. First, we describe the proposed laser's experimental configuration, give the detailed numerical analysis of the proposed CTRC filter and the principle for realizing the SLM operation of the proposed laser. Next, we provide the measured laser characteristics of each obtained laser wavelength, including the optical spectra, wavelength, and power fluctuations, as well as the frequency spectra for confirming SLM operation. Finally, we present the laser linewidth at each obtained wavelength that was measured by the in-house constructed linewidth measurement system based on the laser phase noise demodulation method.

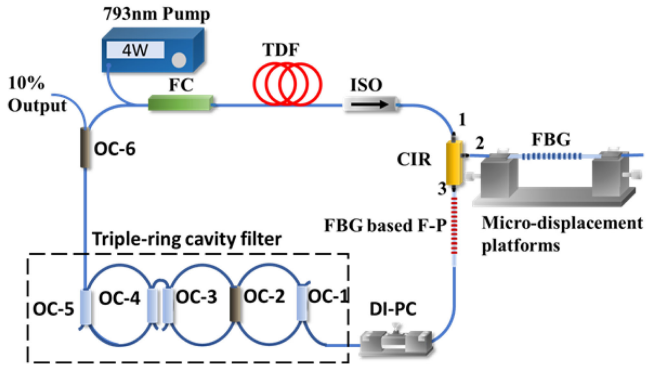

Fig. 1. Schematic diagram of the wavelength-switchable SLM laser with a triple-ring cavity ultra-narrow bandwidth filter.

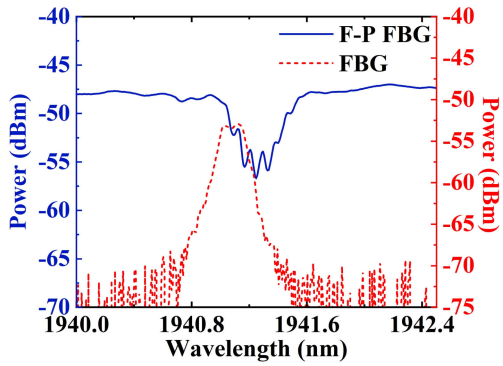

Fig. 2. Transmission spectrum of the FBG based F-P filter and the reflection spectrum of the tunable FBG.

II. Experimental Details

A. Laser Configuration

The experimental setup of the laser is depicted in Fig. 1. A 2.5-m-long Tm-doped double-clad fiber (TDF, Nufern SM-TDF-10P/130-M) was pumped by a laser diode centered at 793 nm with up to 12 W power launched through a fiber combiner (FC). An isolator combined with a circulator ensured the unidirectional oscillation of the laser. Considering that the reflection of the 2 μm band circulator is larger than that in 1550 nm band and the pump power used is relatively high, the isolator is used to avoid the reflected pump power to influence the stability of the pump laser. A narrow bandwidth FBG, clamped by a micro-displacement platform, was connected to port 2, reflecting the specified light to port 3 of the circulator and launching it into the FBG based F-P filter. Here, both the tunable FBG and the F-P filter were fabricated in-house using the phase mask method with the phase mask period of 1347.3 nm, and directly written by a 248 nm KrF excimer laser. The grating length of the tunable FBG was 25 mm. The F-P filter was composed of two 7-mm-long FBGs with 1.6 cm separation. Fig. 2 shows the reflection spectrum of the FBG and the transmission spectrum of the FBG-based F-P filter, which was measured by an OSA (YOKOGAWA AQ6375) with a resolution of 0.05 nm. Five transmission peaks located at ∼1941.12 nm, ∼1941.20nm, ∼1941.29 nm, ∼1941.38 nm and ∼1941.46 nm, with a ∼0.087

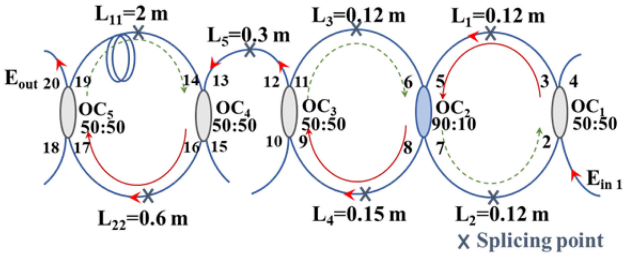

Fig. 3. Schematic diagram of the proposed CTRC filter, where $E_{\text{in }1}$, 2-19, $E_{\text{out-20}}$ denote the coupler (OC_1-OC_5) port numbers, L_1–L_5 and L_{11}–L_{22} indicate the fiber length between two couplers and the sign "X" indicates the splicing point position.

nm separation between two adjacent channels, were dropped in the transmission bandwidth of the F-P filters. Although the transmission depth and bandwidth of each peak were not identical in the spectrum, this does not represent their actual values, as they were limited by the minimum OSA resolution (0.05 nm). By estimation from the laser homodyne RF spectrum, the bandwidth of the transmitting peak was about 0.0126 nm (∼1 GHz). The 3-dB bandwidth of the measured FBG was 0.2 nm. Hence, by gently tuning the micro-displacement platform, the wavelength oscillating in the cavity could be codetermined by the FBG and F-P filter. A subsequent drop-in polarization controller (DI-PC) was incorporated to adjust the laser gain and loss inside the cavity. Then, a CTRC was connected to realize the mode selection and enable the SLM operation of the laser. A 90:10 OC coupled out the resulting SLM lasing from the 10% outcoupling port. The total cavity length of the active main ring cavity was about 10.5 m, corresponding to a ∼20 MHz longitudinal mode spacing.

B. Theory of CTRC Filter and SLM Operation

To realize the SLM operation, the cooperation between the CTRC filter and the narrow-bandwidth F-P filter is essential. First of all, the FSR of the main passband of the CTRC filter should be no less than half of the full-width at half maximum (FWHM) of each transmitting channel of the F-P filter, which allows that only one effective passband of the CTRC constantly is stuck in the FWHM bandwidth of each F-P transmitting peak. Secondly, the FWHM of CTRC filter's each main passband should be 0.5–1 times the spacing between adjacent longitudinal modes of the active main ring cavity [13], [22], which guarantees only one longitudinal mode can pass through the effective passband of the CTRC filter. Both of these two requirements need to be satisfied to ensure SLM oscillation.

Fig. 3 shows a schematic diagram of the proposed CTRC filter, which is composed of a tri-coupler dual-ring (TCDR) cavity filter (OC_1–OC_3) and a dual-coupler ring (DCR) cavity filter (OC_4–OC_5). L_1–L_5 and L_{11}–L_{22} in the diagram represent the fiber length between each connected coupler. 1–20 represent the port of each coupler, while, $E_{\text{in }1}$, E_2–E_{19}, and $E_{\text{out }20}$ denote the corresponding electric field amplitude of each coupler port.

We first analyzed the TCDR filter, whose structure has been proposed and detailed studied in Ref. [21]. The filter transmittance was obtained by substituting the relationship of the nodes among each other and the path and the loop gains of the represented TCRC signal flows into the transmission function which is based on Mason's rule [27]. Here, we briefly give the derived final transmittance T, which is expressed as:

$$\begin{aligned} T_{TCDR} = {} & [\kappa_1\kappa_2\kappa_3(1-\gamma)^3(1-\delta)^2 e^{-2\alpha(L_1+L_4)}]/\ldots \\ & [1+x^2+y^2+z^2-2(x+yz)\cos(\beta(L_1+L_2))\ldots \\ & -2(y+xz)\cos(\beta(L_3+L_4))\ldots \\ & +2xy\cos(\beta(L_1+L_2-L_3-L_4))+2z\cos(\beta L)] \end{aligned} \tag{1}$$

$$\begin{cases} x = (1-\gamma)\sqrt{1-\kappa_1}\sqrt{1-\kappa_2}(1-\delta)e^{-\alpha(L_1+L_2)} \\ y = (1-\gamma)\sqrt{1-\kappa_3}\sqrt{1-\kappa_4}(1-\delta)e^{-\alpha(L_3+L_4)} \\ z = (1-\gamma)^2\sqrt{1-\kappa_2}\sqrt{1-\kappa_4}(1-\delta)^2 e^{-\alpha L} \\ L = L_1+L_2+L_3+L_4 \end{cases} \tag{2}$$

where γ, δ, and α represent the insertion loss, fusion splicing loss, and fiber loss coefficient, respectively; $\kappa_i, i = 1, 2, 3$ denotes the coupling ratio of each coupler; $\beta = 2\pi n_{eff}/\lambda$ is the fiber propagation coefficient; $n_{eff}$and λ are the effective refractive index of the SMF and wavelength, respectively.

The output of the TCDR filter presents a series passband with fixed mode spacing. The bandwidth of each passband and the spacing between them can be optimized by adjusting the fiber length of this proposed compound cavity and the coupling ratio of each coupler. A longer cavity length leads to a narrower bandwidth of each passband and a smaller mode spacing. A lower cross-coupling ratio results in a lower transmittance and narrower passband bandwidth. Since the light in the TCDR can undergo both constructive and destructive interference, by combining and optimizing the coupling ratio and cavity length, a series of the main resonating peaks with a suitable bandwidth and desired main resonating mode spacing can be obtained. A high suppression ratio (SR) ($SR = A_{first-side-peak}/A_{main-peak}$), the ratio between the amplitude of the first adjacent side peak and the main resonating peak, is required for a good filtering effect [22].

Given the previously measured parameters, the separation between adjacent transmission channels of the F-P filter is about 0.087 nm (∼6.928 GHz), and the bandwidth of each channel is about 0.0126 nm (∼1 GHz). According to the Vernier effect [22], when the cavity length difference between the two rings of TCDR is much less than their cavity lengths, the mode spacing TCDR can be given as $FSR = c/(n_{eff} \cdot \Delta L)$, where c is the speed of light, and $\Delta L$is cavity length difference. Considering the first requirement for SLM and the cavity length accuracy of TCDR in practical fabrication, we set ΔL to 3 mm, which corresponds to a 6.94 GHz FSR of TCDR ($c = 3\text{x}10^8$ m/s, $n_{\text{eff}} = 1.44$).

Generally, a smaller coupling ratio of couplers in compound filters is preferred to provide a narrower passband bandwidth, while a lower transmittance. The low transmittance of the filter used in Er-doped fiber lasers may not have a significant impact on their output performance, but is detrimental for a

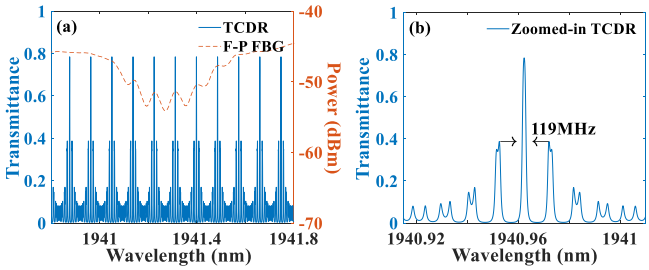

Fig. 4. (a) The simulated spectrum of the proposed TCDR filter and the transmission spectrum of the F-P filter. (b) The zoomed-in spectrum over one mode-spacing of the simulated TCDR.

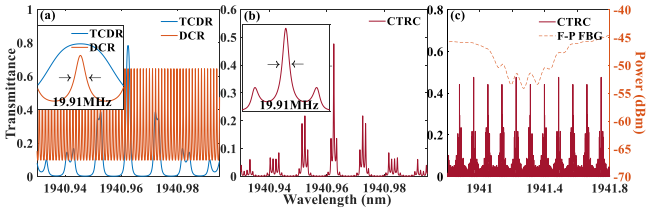

Fig. 5. (a) The simulated transmission spectrum of the DCRC filter and the transmission spectrum of the TCDR filter within a one-mode spacing range; the inset is the zoomed-in spectrum within the range of the main resonating passband. (b) The simulated transmission spectrum of the CTRC filter over one mode-spacing range; the inset is the zoomed-in main resonating peak of the CTRC. (c) The simulated transmission spectrum of the CTRC filter and the transmission spectrum of the F-P filter.

thulium-doped fiber laser as the light in 2 μm band suffers much higher transmission loss. The large cavity loss brought by this low transmittance will lead to laser instability and even no lasing. For this reason, we have to improve the transmittance of the filter used in the proposed laser, meanwhile, a high SR need to be taken into the consideration as well for a better filtering performance. After making the trade-off between the transmittance, the bandwidth of the main resonating peak, and the SR, the coupling ratios of OC_1-OC_3 in TCDR are optimized to 0.5, 0.1, and 0.5, respectively. For OC_2, the large coupling arm is connected to the second ring. The length of each cavity in the TCDR is chosen as 24 cm and 27 cm. The simulated spectra of the TCDR are plotted in Fig. 4.

In Fig. 4(a), the resulting main resonating peaks from the TCDR are well located at each transmission peak maximum. Each main resonating peak has a transmittance of about 0.8 with an SR of ∼0.5, ensuring a good filtering ability; however, using the determined parameters, the bandwidth of the main resonating peak is around 119 MHz, which is much broader than the 20 MHz FSR of the main laser cavity. This allows several modes within the main transmission passband. Hence, a DCR filter is combined with the TCDR to narrow the main peak's bandwidth further.

In the schematic of CTRC in Fig. 3, the input port 13 of the DCR filter is directly connected to the TCDR output port 12, where L_5 is the fiber length between two filters. The field transmission relationship of the output port $E_{out\ 20}$ and input port E_{13} of DCRC is given as [22]:

$$E_{20}/E_{13} = [-(1-\gamma)\sqrt{\kappa_4}\sqrt{\kappa_5}\sqrt{1-\delta}e^{(-\alpha+i\beta)L_{11}}]/\ldots$$
$$[1-(1-\gamma)\sqrt{1-\kappa_4}\sqrt{1-\kappa_5}(1-\delta)e^{(-\alpha+i\beta)(L_{11}+L_{22})}] \tag{3}$$

where $\kappa_i, i = 4, 5$ is the coupling ratio of two couplers; L_{11} and L_{22} are the fiber lengths between couplers. The subsequent transmittance T of DCR is:

$$T_{DCR} = (E_{20}/E_{13})(E_{20}/E_{13})^* \tag{4}$$

Therefore, based on the given transmittances of two filters, their total transmittance can be obtained as:

$$T_{CTRC}$$
$$= T_{TCDR}T_{DCR}(\sqrt{1-\delta}e^{(-\alpha+i\beta)L_5})(\sqrt{1-\delta}e^{(-\alpha+i\beta)L_5})^* \tag{5}$$

To narrow the bandwidth of the main transmission peaks, while also keeping the transmittance and SR as high as possible, we chose higher coupling ratios and longer cavity lengths of the DCRC. After optimization, the coupling ratio of OC_4 and OC_5 are chosen to be 0.5 to obtain a high transmittance, and the cavity length is 2.6 m ($L_{11} = 2$ m, $L_{22} = 0.6$ m).

Fig. 5(a) plots the simulated spectrum of the sole DCRC filter (not connected with the TCDR) in the one-mode spacing range of the TCDR filter. As can be seen, only one resonant peak of the DCRC fall within the main resonant peak of the TCDR, which means that the proposed DCR can further select a mode from the main resonant peak of the TCDR. Fig. 5(b) is the simulated spectrum of the CTRC (the DCRC is connected to the TCDR). The FWHM bandwidth of the main resonant peak decreased from 119 MHz to 19.91 MHz after combining the DCR to the TCDR, and the SR remained at 0.5, indicating good filtering performance. The FSR of CTRC maintains a constant of 6.94 GHz, as determined by the 3 mm $\Delta L$of TCDR. It still matched well with the transmission channels of the F-P filter observing in Fig. 5(c). Furthermore, the 19.91 MHz bandwidth of the main resonant peak is comparable to the 20 MHz FSR of the main laser cavity, which guarantees that only one mode can pass through the main transmission peak of the combined filters. Although it is typically required that the 3-dB passband be 0.5–1 times the FSR, a narrower passband made the laser sensitive to environmental disturbances and even mode-hopping; thus, we did not further narrow the bandwidth of the main transmission peak.

III. Experimental Results

A. Laser Output Characteristics

Based on the simulation analysis above, the CTRC was fabricated strictly using the determined parameters and then spliced into the laser cavity. The experimental results given below prove the good mode selection ability of the proposed CTRC filter. The laser system was deployed together with the pump source on a common optical table and without any professional temperature control and compensation techniques, the experiment was carried out all under a laboratory room temperature with air conditioning constantly running. When the pump power increased to 4 W, stable single-wavelength lasing at 1941.13

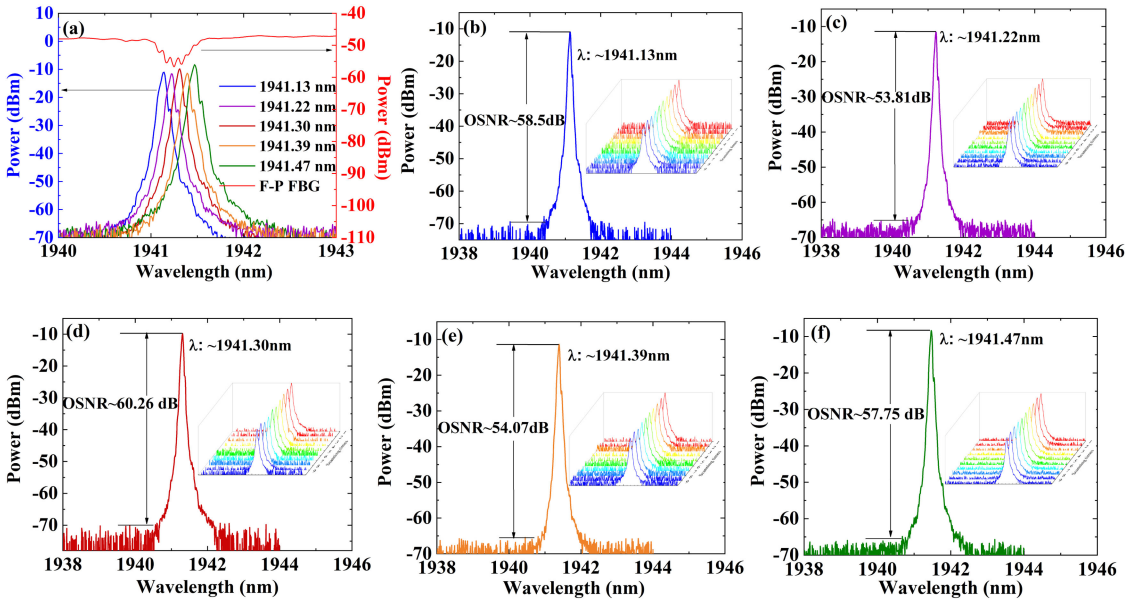

Fig. 6. (a) Spectra of the obtained lasing operating corresponding to each channel of the F-P filter, at wavelengths of (b) 1941.13 nm, (c) 1941.22 nm, (d) 1941.30 nm, (e) 1941.39 nm, and (f) 1941.47 nm. OSNR: optical signal-to-noise ratio.

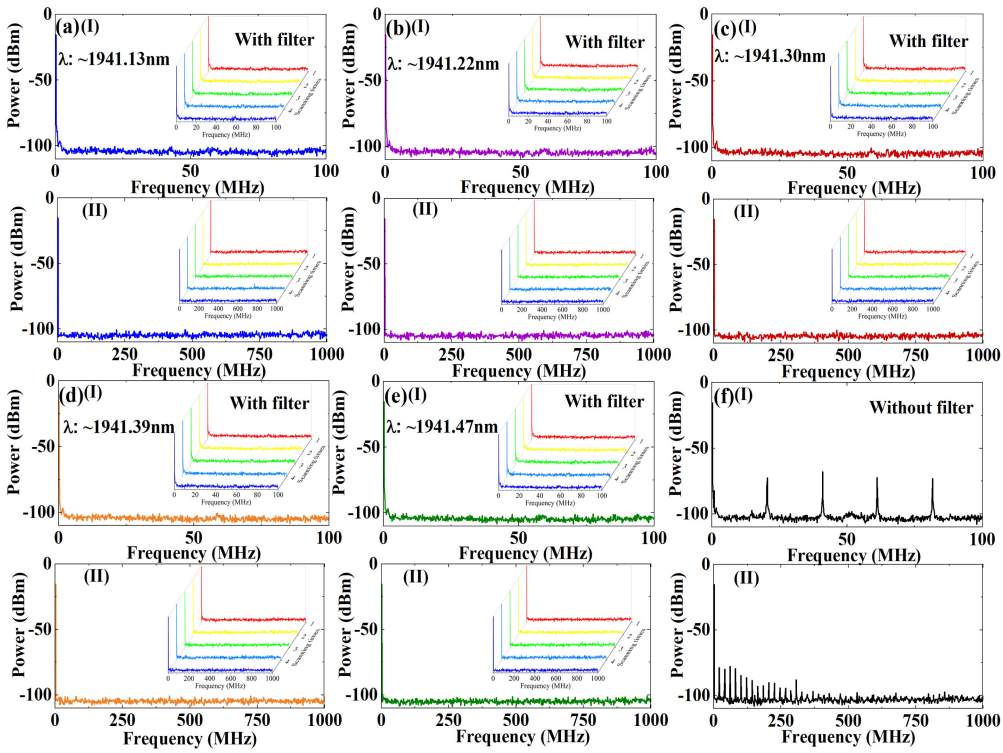

Fig. 7. The self-homodyne RF spectra measured by ESA for each lasing wavelength at (a) 1941.13 nm, (b) 1941.22 nm, (c) 1941.30 nm, (d) 1941.39 nm, (e) 1941.47 nm of proposed five-wavelength switchable SLM laser. The (a)–(e), (I) are the RF spectra measured in a range of 0–100MHz, (II) are the RF spectra measured in a range of 0-1GHz. The insets are the RF beating spectra measured every 10 mins. (f) is the RF beating spectra of the laser without CTRC filter.

nm, 1941.22 nm, 1941.30 nm, 1941.39 nm, and 1941.47 nm with ∼0.13% slope efficiency was obtained by tuning the FBG to each transmission channel of the F-P filter. As shown in Fig. 6(a) , the five lasing wavelengths coincided with the central wavelength of each F-P transmission channel. Fig. 6(b)-(f) are the spectra of each lasing wavelength measured by OSA with a 0.05 nm resolution. Each inset is 10-times repeated OSA scans at 10 min intervals. The 3dB-bandwidth of each lasing wavelength was 0.03 nm, which is below the OSA resolution. The optical signal-to-noise ratios (OSNRs) are all higher than 50 dB. Table. I shows the medium-term operating stability over 90 min at each lasing wavelength, which shows that the laser operates with good

TABLE I
WAVELENGTH AND POWER FLUCTUATIONS OVER 90 MIN

Wavelength (nm)	Wavelength fluctuations (nm)	Power fluctuations (dB)
1941.13	0.01	1.510
1941.22	0.01	0.998
1941.3	0.01	3.006
1941.39	0.00	1.360
1941.47	0.01	0.546

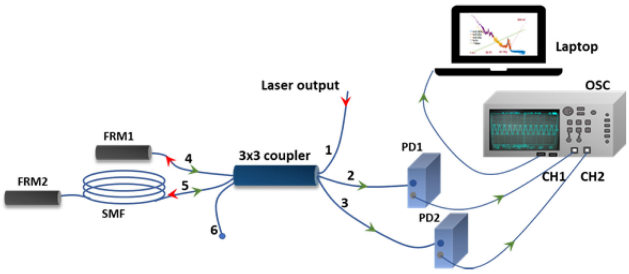

Fig. 8. Configuration of the linewidth measurement system, FRM: Faraday rotation mirror, PD: photodetector, CH: channel.

wavelength stability, and the maximum wavelength fluctuation is 0.01 nm. Since no vibration isolation techniques were employed, and the laser system was placed together with the pump source on the same table, the intense vibration generated from the pump source led to the relatively high power fluctuations (minimum 0.546 dB, maximum 3 dB). Moreover, the relative intensity noise of the pump source also might cause the fluctuations of laser power.

The longitudinal-mode characteristics of the laser at each lasing wavelength were investigated by the self-homodyne method. The measurement setup included a 1 GHz photodetector (Thorlabs PDB470C) and an 8 GHz radio-frequency (RF) electrical spectrum analyzer (ESA, Keysight N9010A). The measured RF spectra of each lasing wavelength are shown in Fig. 7(a–e), where the scanning ranges were set to 0–100 MHz and 0–1 GHz. The insets are the RF beating spectra measured every 10 mins. We can see that there was no beating signal captured for every lasing wavelength, and the laser operated in a stable SLM state. To verify the capability of the CTRC filter, the RF beating spectra of the laser without the CTRC filter spliced inside the cavity were measured for every single-wavelength operation and shown in Fig. 7(f). The numerous spikes in the spectra indicate lasing in multi-longitudinal modes. The spacing of adjacent peaks is about 20.3 MHz, corresponding to a laser cavity length of 10.4 m for the MRC. Furthermore, from Fig. 8(f)(II), the amplitudes of the beat notes above 500 MHz were relatively low, which indicates that the bandwidth of the transmission channel of the F-P filter is about 1 GHz.

B. Laser Linewidth Measurement

The linewidth of each lasing wavelength was measured based on the phase noise demodulation method. The configuration of the measurement system is depicted in Fig. 8. A 3x3 coupler and two Faraday rotation mirrors (FRMs) composed an imbalanced

TABLE II
FWHM LINEWIDTH FOR EACH WAVELENGTH AT DIFFERENT MEASUREMENT TIMES

t (s)	0.001	0.01	0.1	1
$\Delta\nu_{\lambda 1}$ (kHz)	7.694	35.020	45.285	809.69
$\Delta\nu_{\lambda 2}$ (kHz)	5.380	32.375	76.708	787.44
$\Delta\nu_{\lambda 3}$ (kHz)	5.129	27.693	126.970	786.55
$\Delta\nu_{\lambda 4}$ (kHz)	5.162	33.411	68.239	454.16
$\Delta\nu_{\lambda 5}$ (kHz)	7.921	43.447	85.843	730.39

$\lambda_1 = 1941.13$ nm; $\lambda_2 = 1941.22$ nm; $\lambda_3 = 1941.30$ nm; $\lambda_4 = 1941.39$ nm; $\lambda_5 = 1941.47$ nm.

Michelson interferometer (MI). The selected lasing launched into port 1 was spliced through the 3x3 coupler into arm 4, arm 5, and an unused arm 6. A 50-m-long SMF was inserted into arm 5 as the delay line, which introduced a time delay τ between the two arms. After being reflecting by the two FRMs, the light in the arms returned to the coupler, underwent interference, and was then fed into PD1 and PD2 through arm 2 and arm 3. The received interference fringes, containing information about the differential phase fluctuation accumulated in the delay time τ of the MI, were uploaded by the OSC to a computer to calculate the power spectral density (PSD) of the laser's instantaneous phase fluctuation $S_\varphi(f)$ and frequency fluctuation$S_v(f)$ [28].

The laser linewidth could then be calculated using the β-separation line method ($\beta = S_v(f) = (8\ln 2/\pi^2)\cdot f$). By calculating the geometrical area A under the frequency noise PSD obtained for all Fourier frequencies exceeding the β-separation line, the FWHM laser linewidth at different integration bandwidths was approximated using the relation: $FWHM = \sqrt{8\ln 2A}$ [29].

Fig. 9(a)–(e) are the measured frequency noise PSD and the calculated FWHM laser linewidth for each lasing wavelength. Due to the limited dynamic range of the data acquisition system, the experimentally measured total frequency noise PSD was spliced by four segments of the frequency noise PSD measured under different time scales (1 s, 0.1 s, 0.01 s, 0.001 s). In addition, since the data acquisition card we used here is an 8-bit digital OSC, the quantization noise is relatively large, which introduced a horizontal noise base on the right side of each frequency noise PSD spectrum after phase demodulation. To avoid ambiguities due to this system noise, we removed the noise base tails of the frequency noise PSD spectra measured at $t = 0.001$ s, $t = 0.01$ s, and $t = 0.1$ s but kept the noise base at $t = 1$ s. It can be seen from each spectrum that the overlap between the four frequency noise PSD segments was consistent. The FWHM linewidth of each wavelength increased upon increasing the measurement time (decreased integration bandwidth). Table II lists the linewidths for the five lasing wavelengths at different measurement times. At the minimum measurement time (0.001 s), the laser linewidths did not exceed 8 kHz. At the longest measurement time (1 s), the laser linewidths did not exceed 810 kHz. Here, the linewidths at the maximum measurement time were abnormally large, corresponding to the sharp increase at $t = 0.1$ s (100 Hz frequency) in Fig. 10. This was mainly caused by technical noise generated from environmental vibrations and disturbances in the low-frequency range. Moreover, the ~7 kHz

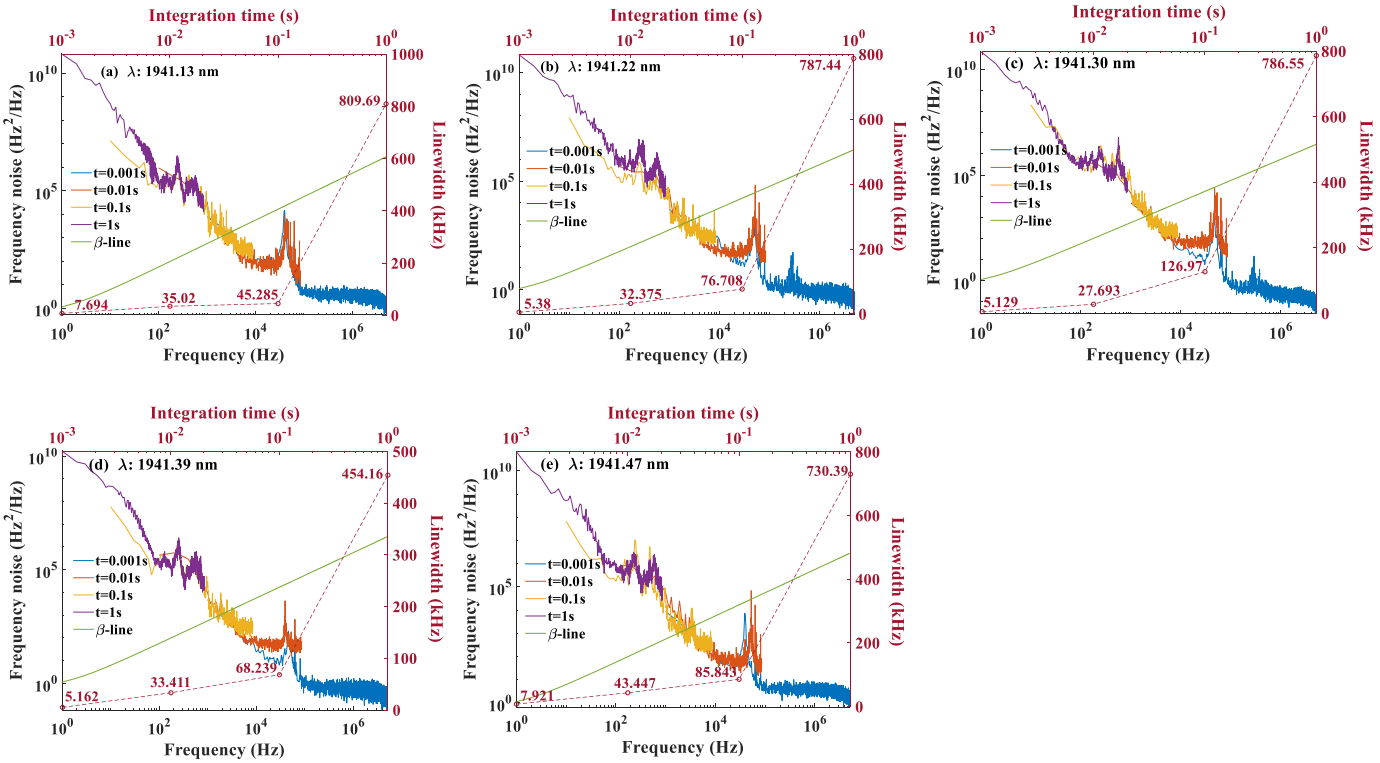

Fig. 9. The frequency noise PSD and the FWHM linewidths at the integration times from 0.001s to 1s for five wavelengths 1941.13nm–1941.47nm.

linewidths at the minimum measurement time were mainly due to thermal noise, as the thermal effect induced by the cladding pumping was more significant than core pumping. The 4-W pump power was high enough to heat the fiber and increase the thermal noise in our case. The relatively low slope efficiency of our laser also led to a more extensive non-Langevin heat source in the gain fiber, which also increased the low-frequency thermal noise of the laser, Nevertheless, the linewidths of the five wavelengths of our laser were remarkably narrower than in other works [11], [30], [31].

IV. Conclusion

Here, we experimentally proposed a five-wavelength switchable SLM thulium-doped fiber laser using an F-P filter as the five-wavelength channel transmitting filter and a CTRC filter as the SLM selector. Wavelength-switching was realized by tuning the FBG to the corresponding F-P transmitting channel. The proposed CTRC was theoretically analyzed in detail. We believe this is the first time that this kind of specially-designed compound-cavity-based filter has been used in a 2 μm fiber laser for SLM selection. The injunction use of a CTRC filter and F-P filter allowed the laser to achieve the SLM operation regardless of the lasing wavelength of each transmitting channel. The relatively good laser output performances were also presented in detail. For all five lasing wavelengths, the OSNRs exceeded 50 dB with wavelength fluctuations less than 0.01 nm. Each lasing operated in a stable SLM state, and the linewidths were less than 8 kHz, which are comparable to the SLM laser in this wavelength range. Since an enough narrow bandwidth FBG in 2 μm band is very difficult to fabricate, we had to corporately use the tunable FBG and the F-P filter in our laser configuration as a manner to narrow down the bandwidth of the wavelength channel, otherwise, the tuning range could be further enhanced by utilizing a single narrower bandwidth FBG, as long as the 3 dB bandwidth of the FBG is comparable with (normally less than the two times of) the effective FSR of the cascaded triple-ring cavity filter. There are also some drawbacks of our laser, i.e., a relatively high power fluctuation and a low slope efficiency. The low laser efficiency was mainly contributed by the high insertion loss of the CTRC filter, and other limiting factors, for instance, the relatively low coupling ratio of the laser output coupler, as well as the field mismatching loss during fusion splicing between the hexagonal cross-section TDF and the common SMF pigtail of the FC and the isolator. Although we have managed to keep the transmittance of the effective passband as high as possible, the power of light after transmitting through all the filters, would still be significantly attenuated. Furthermore, the fiber length of each subring of the TCDR filter is relatively short, which is beneficial to achieve the desired effective FSR. But that leads to a small diameter ($\sim$8 cm) of subrings and subsequently a high additional bend loss. That further decreases the power of lasing output. Nevertheless, we believe that the power fluctuation can be resolved by employing vibration isolation packaging. The lower slope efficiency can be improved by further optimizing the fiber length of each subring in the TCRC filter and the coupling ratio and position of the laser output coupler.

REFERENCES

[1] S. S. Sané *et al.*, "11 W narrow linewidth laser source at 780nm for laser cooling and manipulation of rubidium," *Opt. Exp.*, vol. 20, pp. 8915–8919, Apr. 2012.

[2] V. Kuhn, D. Kracht, J. Neumann, and P. Weßels, *Er-doped Single-Frequency Photonic Crystal Fiber Amplifier With 70 W of Output Power For Gravitational Wave Detection*, vol. 8237. Bellingham, WA, USA: SPIE, 2012.

[3] T. Wu *et al.*, "Observation and optimization of 4He atomic polarization spectroscopy," *Opt. Lett.*, vol. 38, pp. 986–988, Mar. 2013.

[4] G. Canat *et al.*, "High peak power single-frequency MOPFA for lidar applications," in *Proc. Conf. Lasers Electro-Opt.*, San Jose, CA, 2016, Art. no. AM3K.4.

[5] N. Y. Voo, J. K. Sahu, and M. Ibsen, "345-mW 1836-nm single-frequency DFB fiber laser MOPA," *IEEE Photon. Technol. Lett.*, vol. 17, pp. 2550–2552, Dec. 2005.

[6] X. Guan *et al.*, "High-efficiency sub-watt in-band-pumped single-frequency DBR Tm3+-doped germanate fiber laser at 1950 nm," *Opt. Exp.*, vol. 26, pp. 6817–6825, Mar. 2018.

[7] S. D. Lim, J. Yoo, and S. K. Kim, "Widely tunable watt-level single-frequency tm-doped fiber ring laser as pump for Mid-IR frequency generation," *IEEE Photon. J.*, vol. 8, pp. 095105, Jun. 2016, Art no. 1502006.

[8] Q. Li *et al.*, "A single-frequency, ring cavity Tm-doped fiber laser based on a CMFBG filter," *Laser Phys. Lett.*, vol. 10, 2013, Art. no. 095105.

[9] F. Yan, W. Peng, S. Liu, T. Feng, Z. Dong, and G. Chang, "Dual-wavelength single-longitudinal-mode tm-doped fiber laser using PM-CMFBG," *IEEE Photon. Technol. Lett.*, vol. 27, pp. 951–954, Jan./May 2015.

[10] X. He, X. Fang, C. Liao, D. N. Wang, and J. Sun, "A tunable and switchable single-longitudinal-mode dual-wavelength fiber laser with a simple linear cavity," *Opt. Exp.*, vol. 17, pp. 21773–21781, Nov. 2009.

[11] T. Yin, Y. Song, X. Jiang, F. Chen, and S. He, "400 mW narrow linewidth single-frequency fiber ring cavity laser in 2 um waveband," *Opt Exp.*, vol. 27, pp. 15794–15799, May 2019.

[12] M. Zhou, G. Stewart, and G. Whitenett, "Stable single-mode operation of a narrow-linewidth, linearly polarized, erbium-fiber ring laser using a saturable absorber," *J. Lightw. Technol.*, vol. 24, pp. 2179–2183, 2006.

[13] S. Feng, Q. Mao, Y. Tian, Y. Ma, W. Li, and L. Wei, "Widely tunable single longitudinal mode fiber laser with cascaded fiber-ring secondary cavity," *IEEE Photon. Technol. Lett.*, vol. 25, pp. 323–326, Feb. 2013.

[14] J.-F. Lemieux, A. Bellemare, C. Latrasse, and M. Têtu, "100 GHz frequency step-tunable hybrid laser based on a vernier effect between a fabry-perot cavity and a sampled fiber bragg grating," in *Advanced Semiconductor Lasers and Their Applications*, Santa Barbara, CA, 1999, Art. no. 186.

[15] C. Yang *et al.*, "Efficient 1.6 μm linearly-polarized single-frequency phosphate glass fiber laser," *Opt. Exp.*, vol. 25, pp. 29078–29085, Nov. 2017.

[16] C.-C. Lee, Y.-K. Chen, and S.-K. Liaw, "Single-longitudinal-mode fiber laser with a passive multiple-ring cavity and its application for video transmission," *Opt. Lett.*, vol. 23, pp. 358–360, Mar. 1998.

[17] T. Feng *et al.*, "A high stability wavelength-tunable narrow-linewidth and single-polarization erbium-doped fiber laser using a compound-cavity structure," *Laser Phys. Lett.*, vol. 11, Feb. 2014, Art. no. 045101.

[18] T. Feng, F. Yan, S. Liu, Y. Bai, W. Peng, and S. Tan, "Switchable and tunable dual-wavelength single-longitudinal-mode erbium-doped fiber laser with special subring-cavity and superimposed fiber Bragg gratings," *Laser Phys. Lett.*, vol. 11, Nov. 2014, Art. no. 125106.

[19] T. Feng, M. Wang, X. Wang, F. Yan, Y. Suo, and X. S. Yao, "Switchable 0.612-nm-spaced dual-wavelength fiber laser with sub-khz linewidth, ultra-high OSNR, ultra-low RIN, and orthogonal polarization outputs," *J. Lightw. Technol.*, vol. 37, pp. 3173–3182, Jul. 2019.

[20] T. Feng, D. Ding, F. Yan, Z. Zhao, H. Su, and X. S. Yao, "Widely tunable single-/dual-wavelength fiber lasers with ultra-narrow linewidth and high OSNR using high quality passive subring cavity and novel tuning method," *Opt. Exp.*, vol. 24, pp. 19760–19768, Aug. 2016.

[21] T. Feng *et al.*, "Wavelength-switchable ultra-narrow linewidth fiber laser enabled by a figure-8 compound-ring-cavity filter and a polarization-managed four-channel filter,"*Opt. Exp.*, vol. 29, pp. 31179–31200, 2021.

[22] T. Feng *et al.*, "Four-wavelength-switchable SLM fiber laser with sub-kHz linewidth using superimposed high-birefringence FBG and dual-coupler ring based compound-cavity filter," *Opt. Exp.*, vol. 27, pp. 36662–36679, Dec. 2019.

[23] S. Christensen, "Developments in thulium-doped fiber lasers offer higher powers," *Spie Newsroom*, 2008.

[24] S. Fu *et al.*, "Review of recent progress on single-frequency fiber lasers," *J. Opt. Soc. Amer. B*, vol. 34, pp. A49–A62, 2017.

[25] L. Zhang *et al.*, "Six-wavelength-switchable narrow-linewidth thulium-doped fiber laser with polarization-maintaining sampled fiber bragg grating," *Opt. Laser Technol.*, vol. 136, 2021, Art. no. 106788.

[26] W. Han *et al.*, "Wavelength-switchable single-longitudinal- mode thulium-doped fiber laser with sampled fiber Bragg grating," *IEEE Access*, vol. 9, pp. 62212–62218, 2021.

[27] S. J. Mason, "Feedback theory-further properties of signal flow graphs," *Proc. IRE*, vol. 44, pp. 920–926, 1956.

[28] D. Xu *et al.*, "Laser phase and frequency noise measurement by michelson interferometer composed of a 3 x 3 optical fiber coupler," *Opt. Exp.*, vol. 23, pp. 22386–22393, Aug. 2015.

[29] S. Schilt, L. Tombez, G. D. Domenico, and D. Hofstetter, "Frequency noise and linewidth of mid-infrared continuous-wave quantum cascade lasers: An overview," in *The Wonders of Nanotechnology. Quantum and Optoelectronic Devices and Applications*, ch. 12, 2015.

[30] Y. Bai *et al.*, "Demonstration of linewidth measurement based on phase noise analysis for a single frequency fiber laser in the 2 μm band," *Laser Phys.*, vol. 29, May 2019, Art. no. 075102.

[31] J. N. Zhang, W. C. Yao, H. T. Wang, W. Zhou, X. Wu, and D. Y. Shen, "A watt-level single-frequency fiber laser at 2 μm using a silica prolate microresonator," *IEEE Photon. Technol. Lett.*, vol. 31, pp. 1241–1244, Aug. 2019.